Torsional elasticity and energetics of F_1-ATPase

Jacek Czub and Helmut Grubmüller[1]

Department of Theoretical and Computational Biophysics, Max Planck Institute for Biophysical Chemistry, Am Fassberg 11, 37077 Göttingen, Germany

Edited by Axel T. Brunger, Stanford University, Stanford, CA, and approved March 8, 2011 (received for review December 13, 2010)

F_oF_1-ATPase is a rotary motor protein synthesizing ATP from ADP driven by a cross-membrane proton gradient. The proton flow through the membrane-embedded F_o generates the rotary torque that drives the rotation of the asymmetric shaft of F_1. Mechanical energy of the rotating shaft is used by the F_1 catalytic subunit to synthesize ATP. It was suggested that elastic power transmission with transient storage of energy in some compliant part of the shaft is required for the observed high turnover rate. We used atomistic simulations to study the spatial distribution and structural determinants of the F_1 torsional elasticity at the molecular level and to comprehensively characterize the elastic properties of F_1-ATPase. Our fluctuation analysis revealed an unexpected heterogeneity of the F_1 shaft elasticity. Further, we found that the measured overall torsional moduli of the shaft arise from two distinct contributions, the intrinsic elasticity and the effective potential imposed on the shaft by the catalytic subunit. Separation of these two contributions provided a quantitative description of the coupling between the rotor and the catalytic subunit. This description enabled us to propose a minimal quantitative model of the F_1 energetics along the rotary degrees of freedom near the resting state observed in the crystal structures. As opposed to the usually employed models where the motor mechanical progression is described by a single angular variable, our multidimensional treatment incorporates the spatially inhomogeneous nature of the shaft and its interactions with the stator and offers new insight into the mechanoenzymatics of F_1-ATPase.

molecular dynamics | molecular motor | ATP synthase

F_oF_1-ATPase, also known as ATP synthase, is a motor protein whose main biological function is to synthesize ATP from ADP and inorganic phosphate (1). It is a ubiquitous, evolutionary conserved enzyme, present in the bacterial cell membrane, thylakoid membranes of chloroplasts, and the inner membrane of mitochondria. It operates by coupling the ATP synthesis to proton translocation down the transmembrane electrochemical potential gradient. At high ATP concentrations it also operates in reverse direction as an ATP-driven H^+ pump (1–4). This remarkable protein is composed of two oligomeric rotary motors, the membrane-embedded ion-translocating F_o portion and the soluble F_1 part where ATP synthesis/hydrolysis takes place (Fig. 1) (1, 2, 4). The mitochondrial form of F_1 consists of nine polypeptide chains, $\alpha_3\beta_3\gamma\delta\epsilon$ (5, 6). In synthesis mode, each single ion translocation through F_o induces an angular progression of its rotary part, the so-called *c* ring, by one of the 10 to 15 (depending on the species) *c* subunits (4, 7–9). This "power stroke" provides the rotary torque that drives the stepwise rotation of the asymmetric $\gamma\delta\epsilon$ shaft (also called the F_1 "rotor") within the cylinder of hexagonally arranged α- and β-chains that form the enzyme catalytic headpiece, the F_1 "stator" (5, 10, 11). The energy transmitted mechanically by the rotating shaft is used to drive the active sites of F_1 to pass through three distinct conformations that differ considerably in their affinities for the nucleotides (Fig. 1*B*). These cyclic changes drive ATP synthesis and release against highly nonequilibrium intracellular [ATP]/[ADP] concentration ratios (2, 4, 12–15).

Despite the wealth of available data, the mechanistic and structural details of this energy conversion are still not fully understood (2, 4, 13, 14, 16, 17). From a comparison of the proton electrochemical potential difference across a membrane and the free energy of ATP synthesis, it follows that in a living cell at least three to four protons must be translocated through F_o per one ATP molecule synthesized by F_1. This implies that the

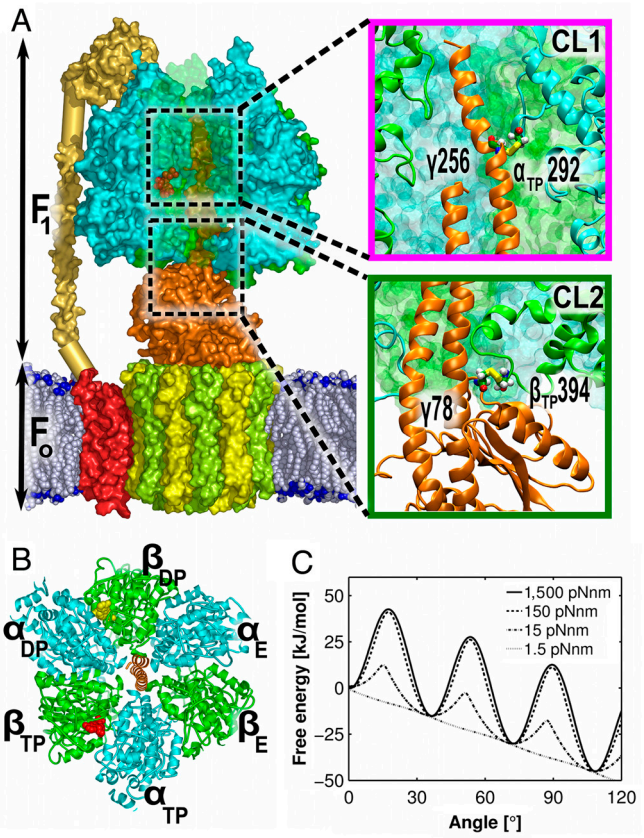

Fig. 1. (*A*) ATP synthase structure and positions of the CL1 (magenta box) and CL2 disulfide (green box) cross-links. F_1: green, β-subunits; cyan, α-subunits; orange, F_1 rotor (subunits $\gamma\delta\epsilon$); F_o: red, *a* subunit, green and yellow, F_o rotor (*c* ring). The portion of F_1 that is located close to the membrane is referred to as the "bottom" portion throughout the text. (*B*) Cross-section of the nucleotide binding domains of F_1 (a view from the membrane). The subunits are labeled as assigned in the original two-nucleotide X-ray structure (5): E, empty binding site; DP, binding site containing ADP; TP, binding site containing ATP; nucleotides are shown as space filling models. (*C*) Smoothening of the driving potential applied to F_1 by the rotating *c* ring with the increasing elastic compliance of the energy transmitting element. As in the original analysis for the reverse reaction (18), it is assumed here that the angular progression of F_1 against a thermodynamic gradient is slow compared to the relaxation of the F_o rotary degree of freedom.

Author contributions: J.C. and H.G. designed research; J.C. performed research; J.C. and H.G. analyzed data; and J.C. and H.G. wrote the paper.

The authors declare no conflict of interest.

This article is a PNAS Direct Submission.

Freely available online through the PNAS open access option.

[1]To whom correspondence should be addressed. E-mail: hgrubmu@gwdg.de.

This article contains supporting information online at www.pnas.org/lookup/suppl/doi:10.1073/pnas.1018686108/-/DCSupplemental.

free energy gained from single-proton steps of the *c* ring must be temporarily stored and accumulated within the enzyme for later use. It is known, from structural studies (11) and kinetic measurements (18), that the actual mechanism of this energy storage further has, first, to allow the enzyme to efficiently perform its function despite the rotational symmetry mismatch between the two motors (4) and, second, to enable the much higher turnover number of the F_oF_1-ATPase holoenzyme than could be expected from the rate measured for the uncoupled F_o and F_1. A quantitative model that meets all these requirements is not yet available.

It has been suggested that a transient energy storage in some torsionally flexible domain(s), e.g., certain regions of the F_1 rotor (in orange in Fig. 1), can meet the above requirements (18–20). Such elastic power transmission may serve as a natural coupling between F_o and F_1 and also would overcome their symmetry mismatch. Additionally, it has been shown that when the energy transmitting element is allowed to undergo elastic deformation then, even though the driving motor progresses in discrete power strokes, the effective driving potential as applied to the coupled motor becomes smooth (Fig. 1*C*) and, consequently, reduces activation barriers (18).

A second possible mechanism of transient energy storage was suggested from molecular dynamics (MD) simulations (21). Accordingly, via a domino-like propagation of structural rearrangements induced by the rotating γ-subunit toward the nucleotide binding sites, a well-concerted sequential retraction of three charged arginine residues from the bound nucleotide was observed (21). This charge separation could account for both transient energy storage and reduced ATP affinity.

To address these issues, the elasticity of a particular region (Fig. 1*A*) of the central shaft was recently probed by introducing disulfide cross-links between the rotor and stator, either at the center or at the bottom (C-terminal domain facing the membrane) of the $\alpha_3\beta_3$ catalytic headpiece (denoted as CL1 and CL2, respectively) (22). By immobilizing the enzyme on a glass plate via the N-terminal β-barrel motifs (at the top of $\alpha_3\beta_3$) the torsional moduli κ ("stiffness") for the two cysteine-substituted mutants, were obtained from the recorded angular fluctuations of magnetic beads rigidly attached to the globular domain of γ. Assuming homogeneous elasticity and neglecting interactions between the rotor and stator, a stiffness of 750 pNnm was found for the region between the two cross-links (22).

The structural origin of the thus obtained elasticity is, however, unknown. Because in the F_1 crystal structures γ is found to interact directly with $\alpha_3\beta_3$, it is unclear to what extent the measured moduli arise from the intrinsic elasticity of the shaft or from its coupling to the catalytic subunit, or both. It is also unknown if the measured elasticity is homogeneously distributed over the considered structural elements. To address these questions, we have used atomistic MD simulations and the fact that the variance of the angular fluctuations is inversely proportional to the elastic modulus and thus also characterizes the local curvature of the underlying free energy surface. Quantifying the elasticity of all relevant F_1 domains then allowed us to determine the intra- and intermolecular contributions to the overall elastic moduli as well as to predict the distribution of elastic energy stored within F_1 in synthesis mode.

Results and Discussion

Central Shaft Elasticity: Comparison with Experiment. To compare the simulation results against the above experiment, we mimicked the setup as closely as possible. To this end, structural models of both the wild type and the two mutants of F_1 (CL1 and CL2 in Fig. 1*A*; for details, see *Materials and Methods*) were established. Immobilization of the enzyme on a surface was modeled by harmonically restraining all backbone atoms of the six N-terminal residues of all β-subunits to their initial positions. Four independent 100-ns equilibrium MD trajectories were generated for each mutant. The fluctuation of the rotation angle for the 2-nm-thick segment of the γ-subunit corresponding to the magnetic bead attachment position was calculated (as described in *Materials and Methods*) for both mutants (Fig. 2*B*; Movie S1 illustrating the rotor angular fluctuation is provided in *SI Text*). As can be seen in Fig. 2*B*, the obtained fluctuation distributions agree quantitatively with the measured distributions. In particular, larger flexibility of the protruding rotor domain is seen for CL1 (Fig. 2, magenta) as compared to CL2 (green) and is attributed here to the angular flexibility of the 3.7-nm portion of the γ-coiled coil between the two linkage positions. Fig. 2*C* shows the computed torsional moduli κ as a function of the length of the used part of the trajectory. As expected, the values decrease with increasing trajectory length, converging to 520 and approximately 1,820 pNnm for CL1 and CL2, respectively, and agree within statistical accuracy with the measured values of 500 and 1,520 pNnm (22). It has been pointed out (23) that these values might slightly overestimate the elastic moduli due to insufficient sampling in the experiment. Similarly, fluctuations slower than our 100-ns simulations time scale might, if present, also render our estimate an upper limit.

Central Shaft Elasticity and Heterogeneity of Torsional Modulus. We extended our analysis beyond the experimentally accessible γ-region toward a spatially resolved characterization of the elastic

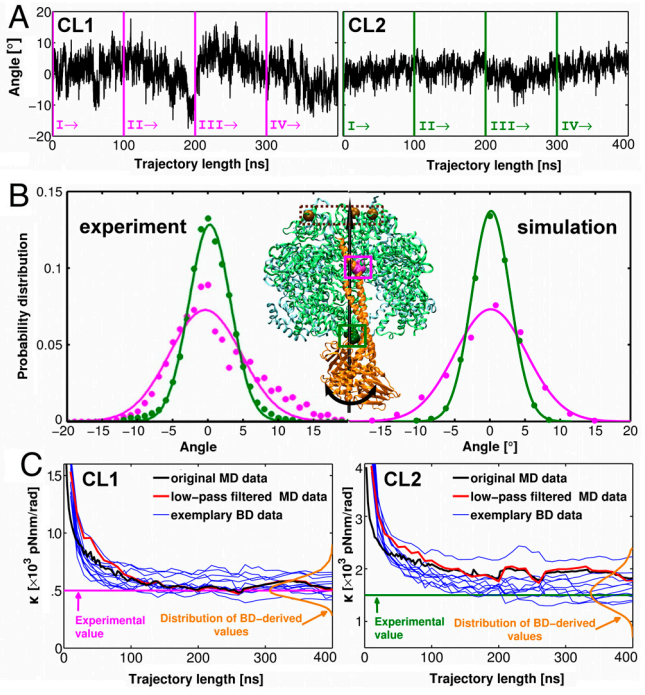

Fig. 2. (*A*) Fluctuation of the rotation angle for the globular domain of the γ-subunit in the CL1-linked (*Left*) and CL2-linked (*Right*) F_1, extracted from four independent simulations (I–IV). (*B*) Comparison of the corresponding fluctuation distributions observed for CL1- (pink) and CL2-linked (green) F_1 in the experiment (18) (*Left*) and in our simulations (*Right*). The symmetry axis of $\alpha_3\beta_3$ (global axis) that was used as the reference axis for angle determination is shown here as a black arrow (*Inset*). The brown spheres at the top of the structure show the location of the restrained N-terminal ends of β-chains. (*C*) Convergence of the torsional modulus κ with increasing length of the trajectory used for analysis. Statistical errors were calculated from the scatter of the κ-values calculated from Brownian dynamics (BD) data (see *SI Text*) and are shown in orange. In addition, the convergence for MD data is shown for which the fastest component, attributed to fast structural rearrangements within the analyzed segment, was filtered out (red).

properties of the whole F_1 complex as well as of the underlying structural determinants.

To characterize the spatial distribution of the torsional elasticity along the F_1 shaft, the rotor subunit was divided into equally-sized segments perpendicular to the $\alpha_3\beta_3$-symmetry axis. For each of these segments, the rotational fluctuation distribution was calculated from the simulations. Fig. 3*A* shows the obtained standard deviations as a function of the distance form the bottom of $\alpha_3\beta_3$, for both cross-linked mutants and for the wild type. To be able to compare the segment elasticities directly, we used, as a reference axis, the vector parallel to the $\alpha_3\beta_3$-symmetry axis passing through each segment center of mass ("local" axis). As opposed to usually applied methods, such an approach captures the flexible nature of the rotation axis in F_1 and guarantees that the elasticity profiles are independent on varying distance of the segment from the arbitrary reference axis.

The fact that the angular fluctuations do not increase with the square root of the distance from the attachment point implies that the torsional elasticity is not uniformly distributed along the shaft but rather exhibits a marked and unexpected heterogeneity. The nonmonotonic behavior of the elasticity profiles obtained for the two mutants and, in particular, the presence of a pronounced minimum at approximately 1.0 nm for CL1 suggest that the observed heterogeneity is in part due to strong interactions between the rotor and the C-terminal helix–turn–helix motifs of α and β in the region $-0.5\ldots+2.5$ nm. For the wild type a similarly reduced angular flexibility is observed, with increasing fluctuations toward both ends of the shaft. Between 0.5 and 2.5 nm similar fluctuations are found for all three systems, indicating that the strong noncovalent coupling to $\alpha_3\beta_3$ might actually be the major factor governing the rotational elasticity of γ in this region. Because of this rotor–stator coupling, the fluctuations observed for the globular portion of the rotor are independent on whether or not the $\alpha_3\beta_3$-penetrating portion is attached covalently, via the CL1 linkage, to the catalytic subunit.

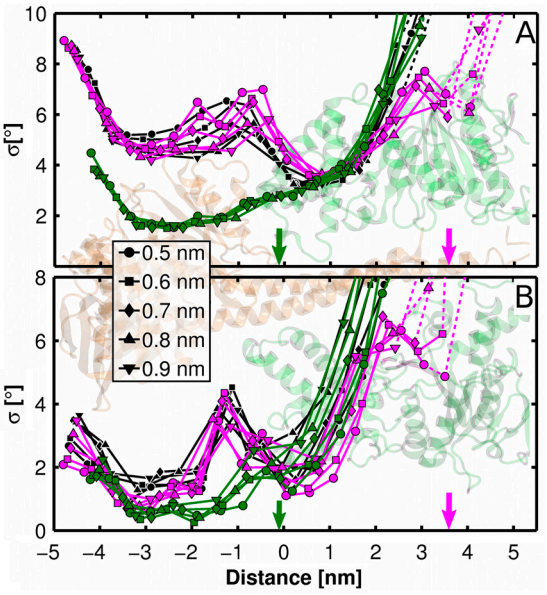

Fig. 3. Variations in the amplitude (standard deviation, σ) of angular fluctuations along the rotor calculated for the wild-type (black) and the CL1- (magenta) and CL2-linked (green) F_1-ATPase using the local axis as the reference vector. The arrows show the positions of the two disulfide cross-links. The fluctuations were obtained either with respect to the torsionally stiff β-barrels at the top of the structure (*A*, "absolute" picture) or with respect to the segment lying directly above the analyzed one (*B*, differential picture). All elasticity profiles have been obtained for five different divisions of the rotor differing in the segment thickness (0.5–0.9 nm). As can be seen, the resulting profiles are similar except for highly flexible single-helix tip of γ (dashed lines). The position of the segment along the rotation axis is measured as the distance of its COM from the average position of the β-DELSEED motifs with the positive sign toward the top of the structure.

To analyze the heterogeneity of the elastic properties in more detail, in addition to the absolute fluctuations of F_1 we also calculated the differential flexibilities between adjacent segments (Fig. 3*B*; see *Materials and Methods*). These profiles reveal a marked increase of the torsional compliance at the very bottom of the shaft globular portion, in agreement with the measurements for the F_oF_1 holoenzyme (22). Closer inspection of the simulations shows that the high flexibility that is crucial for the elastic coupling of the two motors mainly arises from reorientations of the ϵ-subunit β-sandwich around the γ-coiled coil. This effect also increases the overall torsional elasticity of the shaft as "sensed" by F_o from the value of 500 pNnm, measured 2 nm from the bottom of the $\alpha_3\beta_3\gamma$ complex (22), to approximately 280 pNnm at the bottom segment of the wild type and the CL1-linked F_1, observed in the simulations.

A second, rather flexible region is located at the boundary of the globular and $\alpha_3\beta_3$-penetrating portions of the rotor. No significant rotational correlations between these two segments are seen in the differential profiles, such that their rotary motions seem to be largely independent. The very central sector of the rotor, at its narrowest part, appears to be the least resistant to torsional stress. Interestingly, for the region $0\ldots+2$ nm the relatively high values in the differential plots do not result in a large increase of the fluctuation range in the integral picture. This suggests a nonlinear behavior and a short-range nature of the rotational correlations, caused presumably by strong interactions with $\alpha_3\beta_3$.

Distribution of Stator Torsional Elasticity. Next, we determined the $\alpha_3\beta_3$-stator contribution to the overall torsional elasticity. We first calculated the spatial distribution of its angular flexibility. To this end, the whole $\alpha_3\beta_3$-subunit, and also each chain separately, was subdivided into 1.0-nm slabs perpendicular to the $\alpha_3\beta_3$-symmetry axis. These slabs were further subdivided concentrically according to the distance from the axis in 1.0-nm steps, and fluctuation distributions for these elements were calculated as described above. Fig. 4 shows, color coded, the standard deviations of the obtained fluctuations. Overall, it is seen that the stator subunit is torsionally much stiffer than the rotor, with the ligand-binding central domains being only slightly (by approximately 0.5°) more flexible than the fixed β-barrels at the top of the structure. The simulations revealed further that the angular fluctuations increase toward the helix–turn–helix (HTH) motifs of the β C-terminal domains, where the largest values ($\sigma = 4.7°$, 4.2°, and 3.2° for β_{TP}, β_{DP}, and β_E, respectively) are seen. In particular, these values are markedly larger compared to the value found for the bulk of the stator (1.7°). Notably, the angular fluctuations observed for the HTH of both β-subunits in the closed conformation (β_{TP} and β_{DP}) are similar to those seen for the rotor segment with which these motifs interact directly ($\sigma \approx 4.3°$). In addition, their fluctuations around the global axis correlate with the rotor motion that also suggests strong interactions and dynamic coupling between rotor and stator in this region.

This coupling, observed here at the rotor resting position, seems to be crucial for the energy transmission from the asymmetric shaft via the hinge-bending conformational transition of β toward the catalytic sites (15, 24). In this case, one would expect that the elastic properties of the β-subunit should depend on its conformational state. We therefore projected the β-trajectories on the eigenvector corresponding to the open-close transition and obtained from the resulting distributions spring constants of 3.5, 3.6, and 1.5 kcal/(mol nm^2) for β_{TP}, β_{DP}, and β_E, respectively. Indeed, β_E is more than twice as flexible along this degree of freedom than the two β-chains in closed conformation.

Structural Determinants of the Coupling Between Rotor and Stator. To investigate the structural basis for the coupling between the central shaft and $\alpha_3\beta_3$, we analyzed the interactions between these subunits in more detail. Fig. 4*A* reveals three main regions of the catalytic headpiece that are in contact with the γ-subunit, the HTH motifs of the $\alpha_3\beta_3$ C-terminal domains as well as an upper and a lower "bearing." The latter (dashed box 1 and 2, respectively) comprise two sets of loops of the central domains. Using a similar segmentation as above, Fig. S1 shows the average interaction energy between γ along the axis of the shaft. Additionally, the formation of hydrogen bonds between these two subunits was monitored using a geometrical criterion (25) (Fig. 4 *C*–*E*; for full data, see Table S1).

Three main regions show strong interactions. In the first one (dashed oval in Fig. 4*D*), located at the very bottom of $\alpha_3\beta_3$, γ interacts with the highly conserved β-subunit DELSEED sequences (D394–D400) and, to a much lesser extent, with their α-equivalents (F403–D411). In this region, mainly β_{TP} and β_{DP} contribute to the coupling between the rotor and the stator. Via acidic residues of the DELSEED sequences, these two chains form stable H bonds and salt bridges to the conserved loop S73–V85 and to positively charged residues located at the upper surface of the γ-globular portion. Indeed, almost during the entire simulation, Eβ_{TP}395 is H bonded to the backbone amide groups of the Lγ77, Gγ79, and Cγ78; similarly, Dβ_{DP}394 forms a stable hydrogen bond to Rγ133, and Rγ75 strongly interacts with Eβ_{TP}395 and Dβ_{TP}394. These stable interactions are the main cause for the strong correlation between the rotary motion of the flexible β HTH motifs and the neighboring rotor segment around the global axis. Also α_E interacts with γ in this region, e.g., via H bonds between Dα_E411 and Rγ33. These strong couplings may explain the puzzling finding that F_1 with γ truncated to its globular domain is still able to generate rotary torque (26).

The second strongly interacting region (dashed oval in Fig. 4*C*) is located approximately 2 nm above the average DELSEED location. Here, the $\alpha_3\beta_3$-penetrating portion of γ interacts with the upper helices of the HTH motifs, particularly, of the β_{DP} and α_E chains, with H bonds formed between Rγ8 and Dβ_{DP}386. The third region, the lower bearing, interacts with the end of the double-helix part of the γ-coiled coil. Here, all stator chains, particularly β_E, interact considerably with γ. In contrast, the upper bearing does not contribute markedly to the rotor–stator interaction.

Minimal Model of F_1 Torsional Elasticity. The heterogeneously distributed elastic modulus involving the whole protein revealed by our simulations raises the question whether the usually employed single angular variable (12, 15) actually suffices to fully explain the mechanochemistry of F_1. Here, we therefore extend this one-dimensional treatment to a mesoscopic structure-based model. We ask, what is the smallest set of angular variables that quantitatively reproduce the spatial heterogeneity of rotary fluctuations observed in the atomistic MD simulations as well as all measured torsional moduli?

In our model (Fig. 5), the F_1 rotor and stator are represented as a set of harmonically coupled concentric segments oriented perpendicularly to the global axis. Both the division into these segments as well as their coupling constants were obtained from a covariance–matrix-based fluctuation analysis described in *Materials and Methods* and *SI Text*. The model was further optimized to contain only local interactions between the segments.

The resulting model describes the rotor globular portion by three segments (labeled 1–3 in Fig. 5) reflecting the highly nonhomogeneous elasticity of this part. The $\alpha_3\beta_3$-penetrating part is described by segment 4 interacting at the level of HTH motifs (segment 6) and a second segment 5 interacting mostly with the lower bearing (segment 7), thus reflecting the structurally complex nature of the rotor–stator coupling. The highly flexible and relatively weakly interacting γ-tip was not included.

Because our model also describes the local shape of the multidimensional free energy surface that governs the equilibrium fluctuations of the F_1 domains, it allows one to decompose the measured torsional moduli and to assign them to the structural origin (see *Materials and Methods*). For the lower part of the $\alpha_3\beta_3$-penetrating portion (segment 4), the model predicts an effective torsional modulus κ_4 of 620 pNnm. This value agrees with the standard deviation obtained for this segment from MD ($\sigma_4 = 4.5°$) and is consistent with the elastic constant of 750 pNnm that was obtained from the difference of the fluctuations measured at the bottom of the CL1- and CL2-linked mutants and that was previously interpreted as the torsional stiffness of the $\alpha_3\beta_3$-penetrating portion of γ alone (22). In contrast, our model explains this value as arising in approximately 50% and 30% from the coupling of the rotor to the HTH motifs and the lower bearing, respectively, with the intrinsic γ-stiffness contributing the remaining 20%. This decomposition reveals that the coupling to the stator reduces the fluctuation of the thin and relatively elastic $\alpha_3\beta_3$-penetrating part of γ (see Fig. 3) to the effective value as obtained from single-molecule experiments (22). The larger contribution to κ_4 from the coupling to HTH motifs is due to the stronger interactions between γ and $\alpha_3\beta_3$ observed in this region.

Our approach also allows for a separate analysis of the six stator subunits in the HTH region. Qualitatively, when sorted according to decreasing stiffness, an order $\beta_{DP} > \beta_{TP} > \alpha_E >$

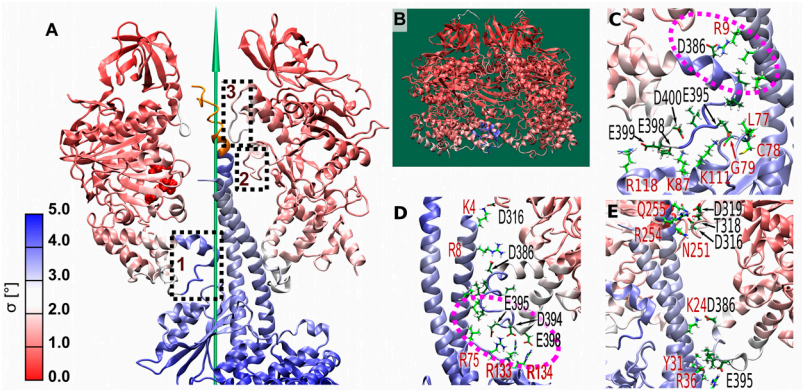

Fig. 4. (*A*) Spatial distribution of the amplitude (standard deviation, σ) of angular fluctuations over the F_1 structure, calculated for the wild-type enzyme with respect to the global axis [for the sake of clarity only β_{TP} (*Left*) and β_E (*Right*) are shown]. Dashed boxes 1, 2, and 3 encompass the stator structural elements responsible for the rotor-stator coupling: HTH motifs, the lower bearing and the upper bearing, respectively. (*B*) Distribution of angular fluctuation within the stator. (*C*–*E*) Interactions between the rotor and the three nucleotide binding chains: β_{TP}, β_{DP}, and β_E, respectively. All pairs of residues forming hydrogen bonds between the rotor and stator with frequency > 0.3 are explicitly denoted in red and black, respectively.

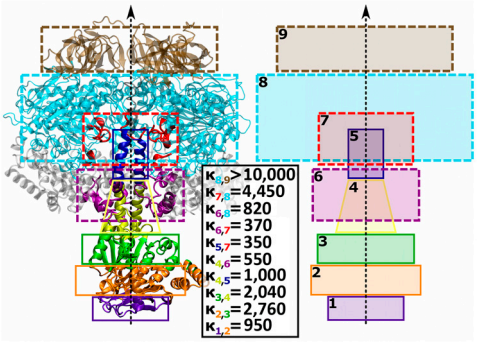

Fig. 5. Sketch of our mesoscopic model of F_1 torsional elasticity, composed of eight harmonically coupled structural segments. In the box the values of the quasiharmonic coupling constants κ_{ij} between the ith and jth segments are listed (in pNnm). The model describes the energetics of F_1 along the rotary degrees of freedom in the vicinity of the free energy minimum corresponding to the rotor angular position as found in most crystal structures.

$\beta_E \gg \alpha_{DP} \approx \alpha_{TP} \approx 0$ is obtained (see *SI Text*). Indeed, and in line with the above interaction analysis, the two closed β-subunits contribute most to the rotor–stator coupling and, thereby, stabilize the angular position of the shaft. Accordingly, as an experimental validation of our model, mutations in the β-regions critical for the coupling (e.g., HTH: Eβ395, Dβ394 Rγ133, and Rγ75; lower bearing: Dβ319, Rγ254) should increase the overall elasticity at the bottom of F_1.

According to the presented model, the overall torsional modulus at the bottom of F_1, κ_1, defined as the effective spring constant corresponding to the fluctuations of the 1.0-nm segment 1 around the global axis, is 280 pNnm. Such an elastic buffer would, however, be too stiff to fully account for the observed lowering of the activation barrier (18). Indeed, an overall torsional modulus for the F_oF_1 holoenzyme of 68 pNnm has been measured (22). Assuming that the c ring is torsionally rigid and, consequently, that the remaining elasticity is provided by the interface between the two motors, one can estimate the elastic modulus of the interface, κ_{int}, to approximately 90 pNnm. Considering, e.g., a 12-subunit c ring, the total elastic energy stored in the structure for progression by a single-proton step of 30° is 2.7 kcal/mol, which agrees well with the energy of 2.8–3.8 kcal/mol provided by the proton-motive force for intracellular conditions. According to our model, approximately 75% of this energy is stored in the interface, approximately 15% in the γ-subunit, and the remaining 10% is distributed at the γ-$\alpha_3\beta_3$ interface and $\alpha_3\beta_3$ itself. Table S2 lists all torsional deformations of the F_1 structural segments and the corresponding elastic energies, calculated for the "flexible" and "rigid" interface with F_o as the two limiting cases.

The simple harmonic model obtained from our simulations suggests that 55% of the total F_o power stroke elastic energy accumulated in F_1 is stored in the shaft globular domain. The main elastic buffer of F_1, storing 30% of the total energy, is located at the very bottom of this domain, in agreement with the single-molecule experiments (22). This buffer is in part due to the above mentioned flexibility of the ϵ subunit, which has been previously shown to participate in the F_o-F_1 coupling (27). Accordingly, we suggest that the role of ϵ-deformation in the elastic power transmission could be tested by cross-link experiments. Further 25% and 15% of the total energy are stored at the γ-$\alpha_3\beta_3$ interface and in the HTH motifs deformed from their equilibrium position, respectively. This coupling, evident especially for β_{DP} and β_{TP} was previously shown to be important for the γ-$\alpha_3\beta_3$ energy transmission when the rotor was displaced from its dwell position using enforced rotation MD simulation (21). Inspection of our trajectories shows that the small-angle deformation of the HTH may propagate along the helix E366–I390 and the β-sheet of the central domain of β_{TP} toward the binding site, thereby weakening the interactions with the bound nucleotide by approximately 10% via a 0.3-nm shift of the Rβ_{TP}191 from the phosphate toward the α_{TP} subunit, as was already reported previously (21). Further destabilization (by approximately 5%) arises from breaking the contact between the adenine moiety and the loop P417–E422 when it is pulled away by the retracted helix D400–L414.

For the $\alpha_3\beta_3$-penetrating and globular portions of the rotor, treated as whole entities, our model predicts overall torsional moduli of 520 pNnm and 120 pNnm, respectively. The unexpectedly small ratio between these values, when compared to a 20–30 ratio one would guess from respective diameters of the two portions, highlights remarkable material properties of the globular domain. Combining the moduli of the two portions, an overall intrinsic stiffness of the F_1 shaft of approximately 100 pNnm is obtained. This value shows that in the analyzed structural state, only 35% of the overall stiffness of F_1, as sensed by F_o or as measured at the bottom of the rotor globular domain, is due to the intrinsic stiffness of the central shaft, whereas the remaining 65% arises from the coupling to the stator.

Assuming that the intrinsic contribution to the measured stiffness is largely independent of the rotor angular position, the only contribution that varies with the rotation angle is the strength of the coupling. Thus, the decomposition provided by our model can serve to measure and to compare the energetics of the rotor–stator coupling between different rotor positions (e.g., dwell states) and, thereby, provides experimental access to the effective potential governing the motion of the γ-subunit in the $\alpha_3\beta_3$-cylinder.

Materials and Methods

Molecular Models. The starting coordinates for the protein were taken from the 2.4-Å crystal structure of the bovine F_1-ATPase covalently inhibited by dicyclohexylcarbodiimide (Protein Data Bank ID code 1E79) (6). The inhibitor itself as well as the glycerol and sulphate molecules were removed, thus leaving only Mg·ATP and Mg·ADP ligands in their respective binding sites. All crystal water molecules were retained. Two short loops missing in the γ-subunit (62–66 and 97–100) were modeled using tCONCOORD (28). The same software was used to form disulfide bonds between the rotor and stator either in the center of the $\alpha_3\beta_3$-cylinder (the cross-link designated as CL1 in Fig. 1*A*) or at the interface between $\alpha_3\beta_3$ and the globular portion of γ (CL2 in Fig. 1*A*). This was done by substituting the selected residues with cysteines, as done in the corresponding experimental study on elastic properties of F_1-ATPase from *Escherichia coli* (22). The corresponding residues were identified by sequence alignment of α-, β-, and γ-chains characterized by, respectively, 56%, 71%, and 30% sequence identity. All the four sites used to introduce the covalent cross-links are conserved. Accordingly, the CL1 linkage was formed between two cysteine residues substituted for γA256 and α_E*E*292 (these substitutions correspond to the *E. coli* F_1 double mutant γ*A*270*C*/α_E*E*284*C*). The CL2 cross-link was formed between the wild-type γC78 and cysteine residue replacing β_{TP}*D*398 (γ*C*87/β_{TP}*D*380*C* in *E. coli* F_1). Note that the introduced covalent bonds did not shift the rotor away from its angular position found in the crystal structure. All the three prepared protein structures (wild-type and the CL1- or CL2-linked mutants) were solvated in a 16.7 × 14.0 × 14.0 nm rectangular unit cell at 140-mM physiological concentration of NaCl.

Simulation Procedure. All MD simulations were performed using Gromacs 4 (29). The protein, its ligands, and ions were modeled using the all-atom OPLS-AA force field (30). Consistently, the TIP4P model was employed to describe the water molecules (31). The simulations were carried out in the NPT ensemble at 300 K and 1 bar using Nosé–Hoover thermostat (32) and Parinello–Rahman barostat (33). Three-dimensional periodic boundary conditions were applied, and the particle mesh Ewald method (34), with a real-space cutoff of 1 nm and an Fast Fourier Transform grid density of 10 nm^{-1}, was used to compute long range interactions. Lennard–Jones interactions were truncated at 1 nm. The length of all covalent bonds in the protein and ligand molecules were constrained using P-LINCS (35). SETTLE (36) was used to constrain the water geometry. The equations of motion were integrated using the leap-frog scheme with a time step of 2 fs. After initial 2-ns runs during which all solute atoms were position-restrained, the systems were further equilibrated for 40 ns under NPT conditions. To ensure stability,

the weak-coupling method (37) was used to control both temperature and pressure during the first 5 ns of equilibration. The initial configurations for the production runs were taken from final 5 ns of equilibration. To achieve better sampling, 4 and 5 independent simulations, lasting 100 and 120 ns each, were performed for the two mutants and for the wild-type enzyme, respectively. Molecular images were created using visual molecular dynamics (VMD) (38) and PyMol (DeLano Scientific).

Angular Fluctuation Analysis. Angular fluctuations for a given protein segment were calculated by minimizing the mass-weighted rmsd from the segment initial configuration using the rotation angle around the reference axis as the single adjustable degree of freedom (DOF). As the reference axis we used either the threefold pseudosymmetry axis of the $\alpha_3\beta_3$-subunit (calculated as the principal axis corresponding to the largest eigenvalue of the $\alpha_3\beta_3$-inertia tensor and passing through the $\alpha_3\beta_3$-center of mass (COM); referred to as the "global" axis) or the same axis but passing through COM of the considered segment (referred to as the local axis). To obtain the "differential" picture, prior to the actual angle determination, the initial fit was performed with the above-lying segment used as the reference group.

The energy stored in an elastic homogeneous rod for a twist angle θ is $V = \frac{1}{2}\kappa\theta^2$, where κ is a torsional modulus (expressed, e.g., in pNnm). This implies that if the rod is tethered at one end and free to undergo thermally driven motion at the other then, in equilibrium, the torsional deformation θ is normally distributed, i.e., $p(\theta) \propto \exp(-\frac{1}{2}\kappa\theta^2/k_BT)$, where k_B is the Boltzmann constant and T is the temperature. Hence the torsional modulus is obtained from fluctuations as $\kappa = k_BT/\sigma^2$, where σ is the standard deviation of a the angular fluctuations, observed either in experiment or in simulation.

Note that for a protein, where θ describes angular fluctuations of a single variable arbitrarily chosen from many DOFs, it is often convenient to consider the free energy of the system as a function of the elastic strain, $G(\theta) = -k_BT\ln p(\theta)$. Accordingly, κ also characterizes the curvature (a second derivative) of $G(\theta)$ in the vicinity of the minimum corresponding to the stable angular position of the rotor and thus directly relates to the average torque driving the rotary motion against the thermodynamic potential gradient.

The generalization of the above for a larger number of DOFs served to obtain our minimal model describing the spatial distribution of the torsional elasticity in the F_1 structure (for details, see *SI Text*). Briefly, in our model F_1 is represented as a set of N harmonically coupled segments. The angular deviation of the ith segment with respect to its equilibrium position is denoted as θ_i. The elastic energy stored in the protein structure due to the set of torsional deformation $\boldsymbol{\theta} = \{\theta_1,\ldots,\theta_N\}$ is $V = \frac{1}{2}\boldsymbol{\theta}^T\mathbf{K}\boldsymbol{\theta}$, where $\mathbf{K}$ is a quasiharmonic Hessian (39) whose entries depend on the "network" of couplings between the segments. The equilibrium probability distribution of $\boldsymbol{\theta}$ is thus given by a multivariate normal distribution, $p(\boldsymbol{\theta}) \propto \exp(-\frac{1}{2}\boldsymbol{\theta}^T\mathbf{K}\boldsymbol{\theta}/k_BT) \propto \exp(-\frac{1}{2}\boldsymbol{\theta}^T\mathbf{C}^{-1}\boldsymbol{\theta})$, where $\mathbf{C}$ is the covariance matrix of angular fluctuations $\langle\boldsymbol{\theta}\boldsymbol{\theta}^T\rangle$, with $k_BT\mathbf{C}^{-1} = \mathbf{K}$.

To determine the model parameters, $\mathbf{C}$ was first computed as the average over MD trajectory for a set of systematically obtained partitions of F_1 into segments. Equating the respective entries of $k_BT\mathbf{C}^{-1}$ with nonzero entries of the assumed form of $\mathbf{K}$, an overdetermined system of linear equations was obtained which was then solved, using the least squares method, for the individual quasiharmonic coupling constants $\{\kappa_{ij}\}$, where i and j are the respective segments. The average over the estimated standard errors of the solution $\{\kappa_{ij}\}$ was used as a criterion to select the model that, within the assumed approximation, optimally reproduces angular fluctuations observed at the atomistic level.

The obtained set of harmonically coupled oscillators determines the shape of the free energy surface $G(\boldsymbol{\theta}) = -k_BT\ln p(\boldsymbol{\theta})$ along the rotary DOFs in the vicinity of the stable structural state. By integrating the joint probability distribution $p(\boldsymbol{\theta}) \propto \exp(-G(\boldsymbol{\theta})/k_BT)$ over all angles except θ_i, one obtains the Gaussian marginal probability distribution $p(\theta_i)$ describing the overall angular fluctuation of the ith segment. From the standard deviation of this distribution σ_i the effective torsional modulus κ_i, i.e., the curvature of the one-dimensional free energy function $G(\theta_i)$, is obtained as a function of individual coupling constants $\{\kappa_{ij}\}$. This relation is then used to decompose the experimentally determined torsional moduli in terms of the relevant DOFs.

ACKNOWLEDGMENTS. We thank Wolfgang Junge for sharing his results with us prior to publication and Carsten Kutzner for helpful discussions. The authors wish to acknowledge funding from the European Union Nanomot (NEST 029084) and European Science Foundation Eurocores Nanocell projects.

1. Boyer P (1997) The ATP synthase—A splendid molecular machine. *Annu Rev Biochem* 66:717–749.
2. Kinosita K, Jr, Adachi K, Itoh H (2004) Rotation of F_1-ATPase: How an ATP-driven molecular machine may work. *Annu Rev Biophys Biomol Struct* 33:245–268.
3. Pu J, Karplus M (2008) How subunit coupling produces the γ-subunit rotary motion in F_1-ATPase. *Proc Natl Acad Sci USA* 105:1192–1197.
4. Junge W, Sielaff H, Engelbrecht S (2009) Torque generation and elastic power transmission in the rotary F_oF_1-ATPase. *Nature* 459:364–370.
5. Abrahams J, Leslie A, Lutter R, Walker J (1994) Structure at 2.8 Å resolution of F_1-ATPase from bovine heart mitochondria. *Nature* 370:621–628.
6. Gibbons C, Montgomery M, Leslie A, Walker J (2000) The structure of the central stalk in bovine F_1-ATPase at 2.4 Å resolution. *Nat Struct Mol Biol* 7:1055–1061.
7. Stahlberg H, et al. (2001) Bacterial Na^+-ATP synthase has an undecameric rotor. *EMBO Rep* 2:229–233.
8. Aksimentiev A, Balabin I, Fillingame R, Schulten K (2004) Insights into the molecular mechanism of rotation in the Fo sector of ATP synthase. *Biophys J* 86:1332–1344.
9. Düser M, et al. (2009) 36 degrees step size of proton-driven c-ring rotation in FoF1-ATP synthase. *EMBO J* 28:2689–2696.
10. Noji H, Yasuda R, Yoshida M, Kinosita K (1997) Direct observation of the rotation of F_1-ATPase. *Nature* 386:299–302.
11. Stock D, Leslie A, Walker J (1999) Molecular architecture of the rotary motor in ATP synthase. *Science* 286:1700–1705.
12. Wang H, Oster G (1998) Energy transduction in the F_1 motor of ATP synthase. *Nature* 396:279–282.
13. Yasuda R, Noji H, Kinosita K, Yoshida M (1998) F_1-ATPase is a highly efficient molecular motor that rotates with discrete 120° steps. *Cell* 93:1117–1124.
14. Gao Y, Yang W, Karplus M (2005) A structure-based model for the synthesis and hydrolysis of ATP by F_1-ATPase. *Cell* 123:195–205.
15. Xing J, Liao J, Oster G (2005) Making ATP. *Proc Natl Acad Sci USA* 102:16539–16546.
16. Yang W, Gao Y, Cui Q, Ma J, Karplus M (2003) The missing link between thermodynamics and structure in F_1-ATPase. *Proc Natl Acad Sci USA* 100:874–879.
17. Dittrich M, Hayashi S, Schulten K (2004) ATP Hydrolysis in the β_{TP} and β_{DP} Catalytic Sites of F_1-ATPase. *Biophys J* 87:2954–2967.
18. Pänke O, Cherepanov D, Gumbiowski K, Engelbrecht S, Junge W (2001) Viscoelastic dynamics of actin filaments coupled to rotary F-ATPase: Angular torque profile of the enzyme. *Biophys J* 81:1220–1233.
19. Junge W, Lill H, Engelbrecht S (1997) ATP synthase: An electrochemical transducer with rotatory mechanics. *Trends Biochem Sci* 22:420–423.
20. Cherepanov D, Mulkidjanian A, Junge W (1999) Transient accumulation of elastic energy in proton translocating ATP synthase. *FEBS Lett* 449:1–6.
21. Böckmann RA, Grubmüller H (2002) Nanoseconds molecular dynamics simulation of primary mechanical energy transfer steps in F_1-ATP synthase. *Nat Struct Biol* 9:198–202.
22. Sielaff H, et al. (2008) Domain compliance and elastic power transmission in rotary FOF1-ATPase. *Proc Natl Acad Sci USA* 105:17760–17765.
23. Wächter A, et al. (2011) Two rotary motors in F-ATP synthase are elastically coupled by a flexible rotor and a stiff stator stalk. *Proc Natl Acad Sci USA*, 108 pp:3924–3929.
24. Cui Q, Li G, Ma J, Karplus M (2004) A normal mode analysis of structural plasticity in the biomolecular motor F_1-ATPase. *J Mol Biol* 340:345–372.
25. Sticke D, Presta L, Dill K, Rose G (1992) Hydrogen bonding in globular proteins. *J Mol Biol* 226:1143–1159.
26. Furuike S, et al. (2008) Axle-less F_1-ATPase rotates in the correct direction. *Science* 319:955–958.
27. Dautant A, Velours J, Giraud M (2010) Crystal structure of the Mg·ADP-inhibited state of the yeast F_1c_10-ATP synthase. *J Biol Chem* 285:29502–29510.
28. Seeliger D, de Groot BL (2009) tCONCOORD-GUI: Visually supported conformational sampling of bioactive molecules. *J Comput Chem* 30:1160–1166.
29. Hess B, Kutzner C, van der Spoel D, Lindahl E (2008) GROMACS 4: Algorithms for highly efficient, load-balanced, and scalable molecular simulation. *J Chem Theory Comput* 4:435–447.
30. Kaminski GA, Friesner RA, Tirado-Rives J, Jorgensen WL (2001) Evaluation and reparametrization of the OPLS-AA force field for proteins via comparison with accurate quantum chemical calculations on peptides. *J Phys Chem B* 105:6474–6487.
31. Jorgensen WL, Chandrasekhar J, Madura JD, Impey RW, Klein ML (1983) Comparison of simple potential functions for simulating liquid water. *J Chem Phys* 79:926–935.
32. Nosé S (1984) A unified formulation of the constant temperature molecular dynamics methods. *J Chem Phys* 81:511–519.
33. Parrinello M, Rahman A (1981) Polymorphic transitions in single crystals: a new molecular dynamics method. *J Appl Phys* 52:7182–7190.
34. Essmann U, et al. (1995) A smooth particle mesh Ewald method. *J Chem Phys* 103:8577–8593.
35. Hess B (2008) P-LINCS: A parallel linear constraint solver for molecular simulation. *J Chem Theory Comput* 4:116–122.
36. Miyamoto S, Kollman PA (1992) SETTLE: An analytical version of the SHAKE and RATTLE algorithm for rigid water models. *J Comput Chem* 13:952–962.
37. Berendsen HJC, Postma JPM, van Gunsteren WF, DiNola A, Haak JR (1984) Molecular dynamics with coupling to an external bath. *J Chem Phys* 81:3684–3690.
38. Humphrey W, Dalke A, Schulten K (1996) VMD: Visual molecular dynamics. *J Mol Graph* 14:33–38.
39. Grubmüller H (1995) Predicting slow structural transitions in macromolecular systems: Conformational flooding. *Phys Rev E* 52:2893–2906.